Editors' Suggestion

Impact Forces of Water Drops Falling on Superhydrophobic Surfaces

Bin Zhang,[1] Vatsal Sanjay,[2] Songlin Shi,[1] Yinggang Zhao,[1] Cunjing Lv,[1,*]
Xi-Qiao Feng,[1] and Detlef Lohse[2,3]

[1]*Department of Engineering Mechanics and Center for Nano and Micro Mechanics,
AML, Tsinghua University, Beijing 100084, China*
[2]*Physics of Fluids Group, Max Planck Center Twente for Complex Fluid Dynamics, and J. M. Burgers Center for Fluid Dynamics,
University of Twente, P.O. Box 217, 7500AE Enschede, Netherlands*
[3]*Max Planck Institute for Dynamics and Self-Organisation, Am Fassberg 17, 37077 Göttingen, Germany*

A falling liquid drop, after impact on a rigid substrate, deforms and spreads, owing to the normal reaction force. Subsequently, if the substrate is nonwetting, the drop retracts and then jumps off. As we show here, not only is the impact itself associated with a distinct peak in the temporal evolution of the normal force, but also the jump-off, which was hitherto unknown. We characterize both peaks and elucidate how they relate to the different stages of the drop impact process. The time at which the second peak appears coincides with the formation of a Worthington jet, emerging through flow focusing. Even low-velocity impacts can lead to a surprisingly high second peak in the normal force, even larger than the first one, namely when the Worthington jet becomes singular due to the collapse of an air cavity in the drop.

In 1876, Worthington [1] published the first photographs of the drop impact process, stimulating artists and researchers alike for almost one-and-a-half centuries. Such drop impacts on solid surfaces are highly relevant in inkjet printing [2], spray coating [3], criminal forensics [4], and many other industrial and natural processes [5–7]. For most of these applications, the drop impact forces, which are the subject of this Letter, can lead to serious unwanted consequences, such as soil erosion [8] or the damage of engineered surfaces [9–11]. A thorough understanding of the drop impact forces is thus needed to develop countermeasures against these damages [12]. Consequently, recent studies analyzed the temporal evolution of these forces [13–19].

These studies were, however, up to now limited to wetting scenarios. Then, not surprisingly, the moment of the drop touchdown [15,20] manifests itself in a pronounced peak in the temporal evolution of the drop impact force, whereas this force is much smaller during droplet spreading [6,21]. For the nonwetting case, i.e., for superhydrophobic surfaces, the droplet dynamics is much richer: after reaching its maximal diameter, the drop recoils [22] and can generate an upward, so-called Worthington jet [1,23]. Ultimately, the drop can even rebound off the superhydrophobic surface [24]. Such spectacular water repellency can occur in nature [25,26] and has technological applications [27–31], including on moving substrates [32], where the droplet dynamics is even richer. The feature of superhydrophobicity, however, is volatile and can fail due to external disturbance such as pressure [26,33–35], evaporation

[36–38], mechanical vibration [39], or the impact forces of prior droplets [40].

In this Letter, we extend the studies on drop impact forces to the impact on superhydrophobic surfaces. Our key result is that then, next to the first above-mentioned peak in the drop impact force at drop touchdown, a *second peak* in the drop impact force occurs, which under certain conditions can be even more pronounced than the first peak. The physical origin of the second peak lies in momentum conservation: when at the final phase of droplet recoil the above-mentioned upward Worthington jet forms, momentum conservation also leads to a downward jet inside the drop [41–44]. It manifests itself in the second peak in the temporal evolution of the force on the substrate. Using both experiments and direct numerical simulations (DNS) [45], we will elucidate the physics of this very rich dynamical process and study its dependences on the control parameters.

Setup.—The experimental setup is sketched in Fig. 1(a). A water drop impacts a superhydrophobic substrate (see Refs. [35,46] for its preparation). We directly measure the impact force $F(t)$ by synchronizing high-speed photography with fast force sensing. In DNS, forces are calculated by integrating the pressure field at the substrate (see Ref. [47] and Supplemental Material Sec. I for details of the experimental and simulation setups [48]). The initial drop diameter D_0 (2.05 mm $\leq D_0 \leq$ 2.76 mm) and the impact velocity V_0 (0.38 m/s $\leq V_0 \leq$ 2.96 m/s) are independently controlled. The drop material properties are kept constant (density $\rho_d = 998$ kg/m^3, surface tension coefficient $\gamma = 73$ mN/m, and dynamic viscosity
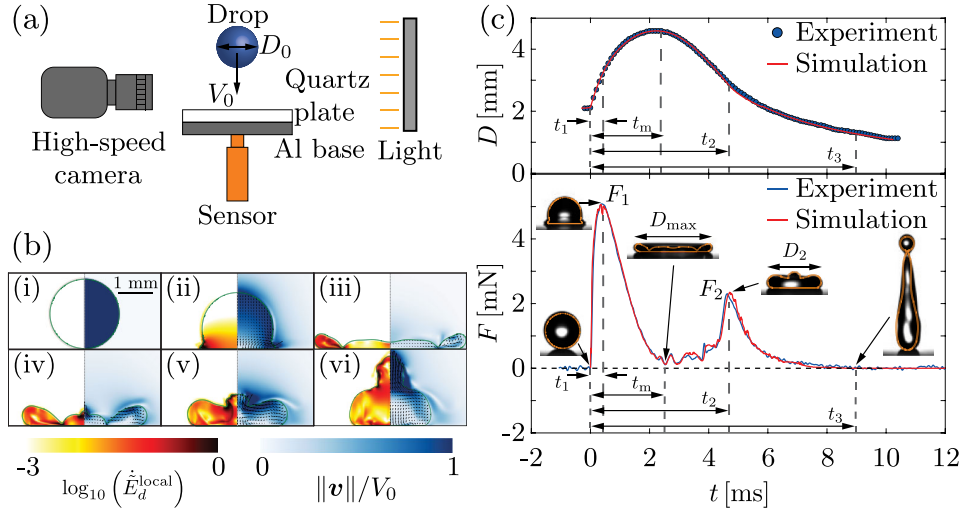
FIG. 1. (a) Experimental setup: a water drop of diameter D_0 impacts on the superhydrophobic quartz plate at velocity V_0. (b) Numerical results for a drop impact dynamics for $D_0 = 2.05$ mm and $V_0 = 1.2$ m/s: $t =$ (i) 0 ms (touchdown), (ii) 0.37 ms, (iii) 2.5 ms, (iv) 3.93 ms, (v) 4.63 ms, and (vi) 5.25 ms. The left part of each numerical snapshot shows the dimensionless local viscous dissipation rates $\dot{\hat{E}}_d^{\text{local}}$ (see Supplemental Material, Eq. S8 [48]) on a $\log_{10}$ scale and the right part the velocity field magnitude normalized with the impact velocity. The black velocity vectors are plotted in the center of mass reference frame of the drop to clearly elucidate the internal flow. (c) Spreading diameter $D(t)$ and impact force $F(t)$ on the substrate as function of time: comparison between experiments and simulations (We = 40). The insets show representative snapshots at specific time instants overlaid with the drop boundaries from simulations in orange, revealing good agreement again. $F_1 \approx 5.1$ mN and $F_2 \approx 2.3$ mN are the two peaks of the normal force $F(t)$ at $t_1 \approx 0.37$ ms and $t_2 \approx 4.63$ ms, respectively. t_m is the moment corresponding to the maximum spreading of the drop and t_3 represents the end of contact ($F = 0$). See Supplemental Movie S1 [48].

$\mu_d = 1.0$ mPa s). All experiments were carried out at ambient air pressure and temperature. The Weber number (ratio of drop inertia to capillary pressure) We $\equiv \rho_d V_0^2 D_0/\gamma$ ranges between 1–400 and the Reynolds number (ratio of inertial to viscous stresses) Re $\equiv \rho_d V_0 D_0/\mu_d \approx 800$ to 10^5. Note that for our simulations, we keep the drop Ohnesorge number (ratio of inertial-capillary to inertial-viscous timescales) Oh $\equiv \mu_d/(\rho_d \gamma D_0)^{1/2}$ constant at 0.0025 to mimic 2 mm diameter water drops.

Formation of a second peak in the force and mechanism thereof.—Figure 1(b) illustrates the different stages of the drop impact process for We = 40, and Fig. 1(c) quantifies the spreading diameter $D(t)$ (the maximum width of the drop at time t) and the normal force $F(t)$ (see Supplemental Movie S1 [48]). Note the remarkable quantitative agreement between the experimental and the numerical data for both $D(t)$ and $F(t)$, giving credibility to both. As the drop touches the surface [Fig. 1(b)(i)], the normal force $F(t)$ increases sharply to reach the first peak with amplitude $F_1 \approx 5.1$ mN in a very short time $t_1 \approx 0.37$ ms [Fig. 1(b)(ii)]. At this instant, the spreading diameter $D(t)$ is equal to the initial drop diameter D_0, $D(t_1) \approx D_0$ [15–19]. Subsequently, the normal force reduces at a relatively slow rate to a minimum (≈ 0 mN) at $t_m \approx 2.5$ ms. Meanwhile, the drop reaches a maximum spreading diameter $D(t_m) = D_{\max}$ [Fig. 1(b)(iii)]. The force profile $F(t)$, until this instant, is very close to that on a hydrophilic surface (see Supplemental Material

Sec. II [48]). However, contrary to the wetting scenario, on superhydrophobic substrates, the drop starts to retract, creating high local viscous dissipation in the neck region connecting the drop with its rim [Figs. 1(b)(iii)–1(b)(iv)]. Through this phase of retraction, the normal reaction force is small, but shows several oscillations owing to traveling capillary waves for 2.5 ms $< t <$ 3.8 ms [Fig. 1(c)]. The drop retraction and the traveling capillary waves lead to flow focusing at the axis of symmetry, creating the Worthington jet [Figs. 1(b)(iv)–1(b)(v)] and hence also the opposite momentum jet that results in an increase in the normal force $F(t)$. Consequently, the hitherto unknown second peak appears, here with an amplitude $F_2 \approx 2.3$ mN and at time $t_2 \approx 4.63$ ms. Lastly, the normal force $F(t)$ decays slowly [Figs. 1(b)(v)–1(b)(vi)] to zero, here finally vanishing at $t_3 \approx 8.84$ ms. This time instant t_3 is a much better estimate for the drop contact time as compared to the one observed at complete detachment from side view images which is about 2 ms longer in this case [24,61]. Therefore, in summary, here we have identified the mechanism for the formation of the second peak in the normal force and four different characteristic times, t_1, t_m, t_2, and t_3 [Fig. 1(c)].

Weber-number dependence of the characteristics times.—Next, we look into the dependence of these times on the impact Weber number We. The instant t_1 of the first peak of the force $F(t)$ scales with the inertial timescale [Fig. 2(a)], i.e., $t_1 \sim \tau_\rho = D_0/V_0$ with different
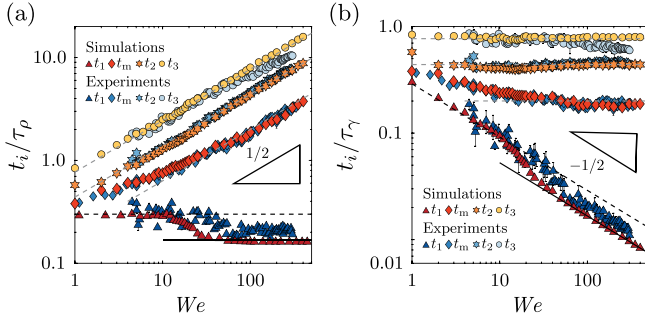
(a)

(b)

FIG. 2. Characteristic times as functions of We. The times t_1, t_m, t_2, and t_3 are normalized by the inertial timescale $\tau_\rho = D_0/V_0$ [in (a)] or by the inertial-capillary timescale $\tau_\gamma = (\rho_d D_0^3/\gamma)^{1/2}$ [in (b)]. The black dashed and solid lines represent $t_1 \approx 0.3\tau_\rho$ and $t_1 \approx 1/6\tau_\rho$, respectively. The gray dashed lines show the best straight line fits to the experimental data, $t_m \approx 0.20\tau_\gamma$, $t_2 \approx 0.44\tau_\gamma$, and $t_3 \approx 0.78\tau_\gamma$.

We-dependent prefactors (≈ 0.3 at low and $\approx 1/6$ at high We, respectively). The solid black line in Fig. 2(a) is the theoretical inertial limit, $t_1/\tau_\rho = 1/6$ [17], and matches our experimental and in particular numerical data. As seen from Fig. 2, the other three characteristic times scale differently with We than t_1. Specifically, t_2 and t_3 become independent of We when rescaled with the inertial-capillary time $\tau_\gamma = (\rho_d D_0^3/\gamma)^{1/2}$ while t_m has a weak We dependence at low We, and becomes We independent only for We $\gtrsim 10$, see Fig. 2(b). The reason for this We-independent behavior is that the impact process is analogous to one complete drop oscillation [24] which is determined by the inertial-capillary time τ_γ [75]. Maximum spreading (t_m) occurs at almost one-quarter of a full oscillation (consistent with our result $t_m \approx 0.20\tau_\gamma$) whereas the complete contact time t_3 takes about one full oscillation (consistent with our result $t_3 \approx 0.78\tau_\gamma$). Finally, the time instant $t_2 \approx 0.44\tau_\gamma$ of the second peak in the impact force coincides with the time when the drop's motion changes from being predominantly radial to being vertical, as this moment is associated with the formation of the Worthington jet [76], pp. 18–20. Note that here for the impact on the superhydrophobic substrate, the duration of nonzero forces (e.g., for We = 40 we find $t_3/\tau_\rho \approx 5.2$ [Fig. 1(c)]) is much longer than that for the impact on a hydrophilic surfaces [17,18], where for the same We = 40 one has $t_3/\tau_\rho \approx 2.0$.

Weber-number dependence of the magnitude of the first peak.—As the drop falls on a substrate, momentum conservation implies $F_1 \sim V_0(dm/dt)$, where the mass flux dm/dt can be calculated as $dm/dt \sim \rho_d V_0 D_0^2$ [14]. As a result, $F_1 \sim \rho_d V_0^2 D_0^2$, as shown in Fig. 3(a) for high Weber numbers (We > 30, $F_1 \approx 0.81\rho_d V_0^2 D_0^2$). This asymptote also matches the experimental and theoretical results of similar studies conducted on hydrophilic substrates [16,17]. Indeed, the first peak force originates from an inertial

shock following the impact of drops onto an immobile substrate and is independent of the wettability. Further, the minimum Reynolds number for the current work is 800, which is well above the criterion (Re > 200) for viscosity-independent results [16,17]. One would expect $\tilde{F}_1 \equiv F_1/\rho_d V_0^2 D_0^2$ to be constant throughout the range of our parameter space. Nonetheless, when We < 30, the data deviates from the inertial asymptote. Such deviations have been reported previously on hydrophilic surfaces as well [14]. Here, inertia is not the sole governing force, and it competes with surface tension. We propose a generalization of the first peak of the impact force to $F_1 = \alpha_1 \rho_d V_0^2 D_0^2 + \alpha_2(\gamma/D_0)D_0^2$, based on dimensional analysis, with α_1 and α_2 as free parameters. From the best fit to all the experimental and numerical data, we obtain $\tilde{F}_1 \approx 0.81 + 1.6\text{We}^{-1}$, which well describes the data, see Fig. 3(a).

Weber-number dependence of the magnitude of the second peak.—We now focus on the second peak F_2 of the impact force $F(t)$. In Fig. 3(b), we show the We dependence of the nondimensional version thereof, $\tilde{F}_2 \equiv F_2/(\rho_d V_0^2 D_0^2)$. We identify four main regimes, namely, I. Capillary (We < 5.3), II. Singular jet (5.3 < We < 12.6), III. Inertial (30 < We < 100), and IV. Splashing (We > 100). The range 12.6 < We < 30 marks the transition from the singular jet to the inertial regime. In regime I (We < 4.5), the amplitudes of both peaks, F_1 and F_2, are smaller than the resolution (0.5 mN) of our force transducer, so we cannot extract the temporal variation of the normal reaction force from the experiments. Capillary oscillations dominate the flow in this regime [77], leading to more than two peak forces, remarkably perfectly identical to what is observed in our simulations [see Fig. 3(d)(i) and Supplemental Movie S2 [48]].

In regime II, with increasing We, there is a sharp increase in the amplitude $\tilde{F}_2$ of the second peak. A striking feature of this regime is that the magnitude of the second peak force exceeds that of the first one, $\tilde{F}_2 > \tilde{F}_1$, see Fig. 3(c) which illustrates the case with the highest second peak force ($\tilde{F}_2 = 2.98$, occurring for We = 9, Supplemental Movie S3 [48]). The large force amplitude in this regime correlates to the formation of an ultrathin and high-velocity singular Worthington jet [23]. Here, the Worthington jet is most pronounced as it results from the collapse of an air cavity as well as the converging capillary waves [see insets of Figs. 3(c) and 3(d)(ii)–3(d)(iii)]. It is reminiscent of the hydrodynamic singularity that accompanies the bursting of bubbles at liquid-gas interfaces [78,79]. Outside regime II such bubbles do not form, see Figs. 3(d)(iv)–3(d)(vi). Consistent with this view, the case with maximum peak force [We = 9, Fig. 3(c)] entrains the largest bubble. Another characteristic feature of this converging flow is that, despite having a small Ohnesorge number (= 0.0025) that is often associated with inviscid potential flow inside the drop [80], it still shows high rates of local viscous dissipation near the axis of symmetry [Fig. 3(c) insets
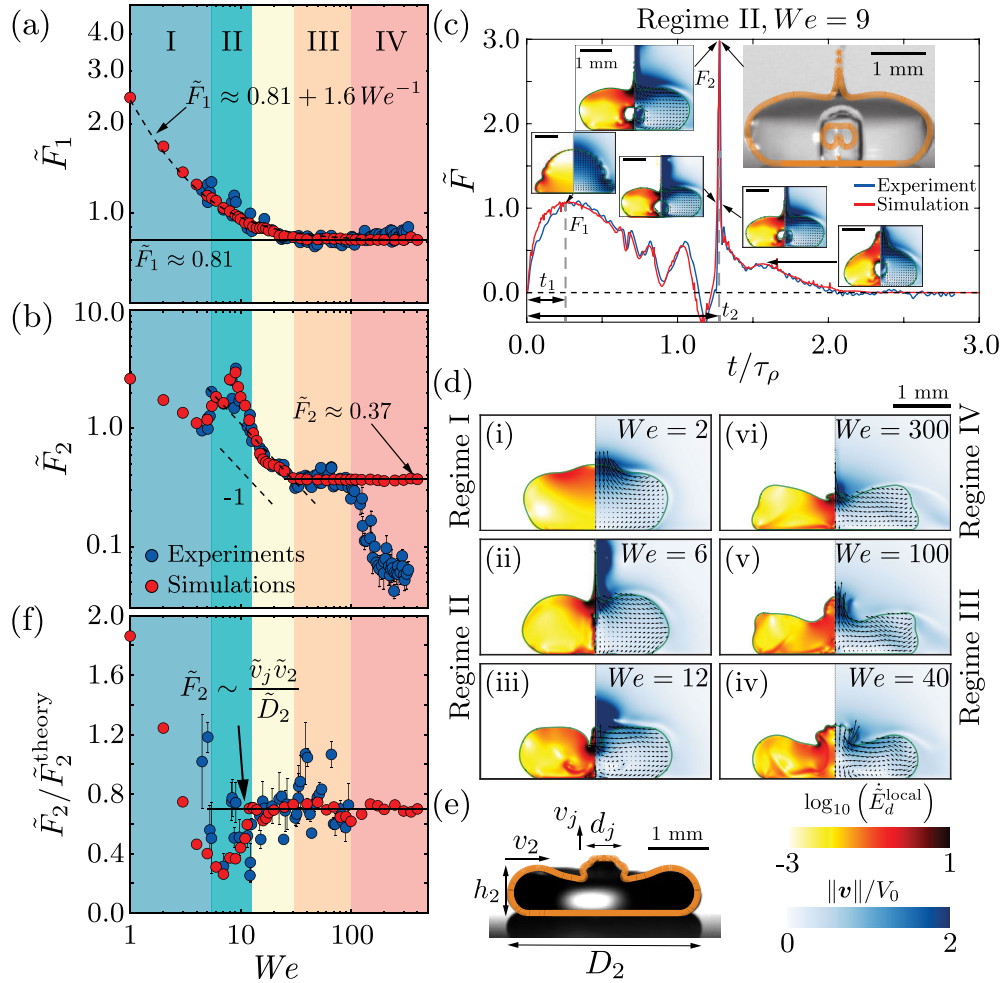
FIG. 3. Dimensionless peak forces, (a) $\tilde{F}_1$, (b) $\tilde{F}_2$ as functions of We. The variation of the second peak force $\tilde{F}_2$ with We divides the parameter space into four regimes: I. Capillary, II. Singular jet, III. Inertial, and IV. Splashing. (c) Evolution of the normal force $F(t)$ of an impacting drop for the case with highest $\tilde{F}_2$ (We = 9). Note again the outstanding agreement between the experimental and the numerical results, including the various wiggles in the curve, which originate from capillary oscillations. The insets show representative snapshots at specific time instants. (d) Numerical snapshots at the instants of the second peak force (t_2) for We = (i) 2, (ii) 6, (iii) 12, (iv) 40, (v) 100 and (vi) 300. The left part of each numerical snapshot shows the dimensionless local viscous dissipation rates $\dot{\tilde{E}}_d^{\text{local}}$ (see Supplemental Material, Eq. S8 [48]) on a $\log_{10}$ scale and the right part the velocity field magnitude normalized with the impact velocity. (e) Experimental drop geometry at t_2 for We = 40 (along with the drop contour from numerics in orange) to illustrate its spreading diameter D_2, height h_2, retraction velocity v_2, jet diameter d_j, and jet velocity v_j. (f) Comparison of the second peak force $\tilde{F}_2$ with its theoretical prediction $\tilde{F}_2^{\text{theory}} = \tilde{v}_j \tilde{v}_2 / \tilde{D}_2$ [Eq. (2)].

and 3(d)(ii)–3(d)(iii)], due to the singular character of the flow (see Supplemental Movie S4).

When We is further increased, we (locally) find $\tilde{F}_2 \sim$ We^{-1} in the transition regime (12.6 < We < 30), followed by $\tilde{F}_2 \sim$ We^0 in the inertial regime III (30 < We < 100). Specifically, by employing best fits, we obtain

$$\tilde{F}_2 = \frac{F_2}{\rho_d V_0^2 D_0^2} \approx \begin{cases} 11 \text{ We}^{-1} & (12.6 < \text{We} < 30), \\ 0.37 & (30 < \text{We} < 100). \end{cases} \quad (1)$$

We will now rationalize this experimentally and numerically observed scaling behavior of the amplitude F_2 of the

second peak using scaling arguments. As already mentioned, Fig. 3(d) shows that the second peak in the force at t_2 coincides with an upward jet, which has typical velocity v_j (see Supplemental Material Sec. IV [48] for calculation details) and typical diameter d_j, Fig. 3(e). Figure 3(d) also illustrates strong radially symmetric flow focusing due to the retracting drop in regimes II and III. We define the recoiling velocity of the drop at time t_2 as v_2, the droplet height at that moment as h_2, and the droplet diameter at that moment as $D_2 = D(t_2)$, see again Fig. 3(e). Note that regime II also includes stronger converging capillary waves and the collapsing air cavity [Fig. 3(c) insets and

Figs. 3(d)(ii)–(d)(iii)]. The presence of the substrate breaks the symmetry in vertical direction, directing the flow into the Worthington jet. Using continuity and balancing the volume flux at this instant t_2, we obtain $v_2 D_2 h_2 \sim v_j d_j^2$. Of course, D_2 and h_2 are also related by volume conservation. Assuming a pancake-type shape at t_2, we obtain $D_2^2 h_2 \sim D_0^3$ [21] and therefore, $v_j d_j^2 \sim v_2 D_0^3 / D_2$. As the drop retracts, the velocity of the flow field far away from the jet is parallel to the base [Fig. 3(d)]. So, the occurrence and strength of the second peak F_2 is mainly a result of the flow opposite to the vertical Worthington jet [Figs. 3(d)(iv)–3(d)(vi)], which naturally leads to $F_2 \sim \rho_d v_j^2 d_j^2$ (momentum flux balance in the vertical direction). Combining the above arguments, we get $F_2 \sim \rho_d v_j v_2 D_0^3 / D_2$ which can be nondimensionalized with the inertial pressure force $\rho_d V_0^2 D_0^2$ to obtain

$$\tilde{F}_2 = \frac{F_2}{\rho_d V_0^2 D_0^2} \sim \frac{\tilde{v}_j \tilde{v}_2}{\tilde{D}_2}, \qquad (2)$$

where, $\tilde{v}_j = v_j / V_0$, $\tilde{v}_2 = v_2 / V_0$, and $\tilde{D}_2 = D_2 / D_0$ are the dimensionless jet velocity, drop retraction velocity, and spreading diameter, respectively, all at t_2.

Figure 3(f) compares the amplitude of the second peak as obtained from the experiments and simulations with the theoretical prediction of Eq. (2) (see Supplemental Material Sec. IV). Indeed, this scaling relation reasonably well describes the transitional regimes II–III and regime III data. Obviously, in regime I, the theoretical prediction is invalid because the hypothesis of flow focusing breaks down, and capillary oscillations dominate the flow, with no Worthington jet occurring [Fig. 3(d)(i)]. Further, Eq. (2) overpredicts the forces in regime II because efficient capillary waves focusing and air cavity collapse lead to extremely high-velocity singular jets. The entrained air bubble also shields momentum transfer from the singular Worthington jet to the substrate [insets of Fig. 3(c)].

We finally come to the very large impact velocities of regime IV. Then, when We $\gtrsim 100$, in the experiments splashing occurs [5], see Supplemental Movie S6 [48]. At such high We, the surrounding gas atmosphere destabilizes the rim [67,68]. Therefore, in regime IV, kinetic and surface energies are lost due to the formation of satellite droplets, resulting in diminishing $\tilde{F}_2$ in the experiments [Fig. 3(b)]. In contrast, for our axisymmetric (by definition) simulations, the above-mentioned azimuthal instability is absent [67] and the plateau $\tilde{F}_2 \approx 0.37$ continues in this regime. Consequently, Eq. (2) holds only for the simulations in regime IV [Fig. 3(f)], and not for the experiments. Further analysis of the experimentally observed fragmentation scenario is beyond the scope of the present Letter. For future work, we suggest that one could also experimentally probe F_2 in this regime by suppressing the azimuthal instability (for instance, by reducing the atmospheric pressure [81]).

Conclusions and outlook.—In this Letter, we have experimentally obtained the normal force profile $F(t)$ of water drops impacting superhydrophobic surfaces. To elucidate the physics and study the internal flow, we have also used direct numerical simulations, which perfectly match the experimental results without any fitting parameter. In the force profile $F(t)$, we identified two prominent peaks. The first peak arises from an inertial shock following the impact of the impacting drop onto the immobile substrate. The hitherto unknown second peak occurs before the drop rebounds. The variation of the amplitude of this peak with Weber number divides the parameter space into four regimes, namely the capillary, singular jet, inertial, and splashing regime. This peak in the force occurs due to the momentum balance when the Worthington jet is created by flow focusing, owing either to capillary waves (singular jet regime) or drop retraction (inertial regime). Surprisingly, even a low Weber number impact (singular jet regime) can lead to a highly enhanced second peak in the force profile, remarkably even larger than the first one, triggered by the singularity occurring at the collapse of an air cavity. Lastly, we have derived scaling relations for these peak forces.

The esthetic beauty of our results on the drop impact dynamics on a nonwetting surface and the forces associated with it lies in the combination of the simplicity and daily-life character of the experiment and the observed rich and surprising phenomenology. The achieved insight is technologically relevant to develop countermeasures to the failure of superhydrophobic materials (e.g., by avoiding the regime $5.3 < \mathrm{We} < 12.6$ or reducing the spacing of the textures [26]). Interesting extensions of our Letter include the study of impact forces of viscous drops (i.e., drops with Oh < 1), which will show quite different scaling behavior [82], and of Leidenfrost drops [83].

---

[*]cunjinglv@tsinghua.edu.cn

[1] A. M. Worthington, Proc. R. Soc. London, Ser. A **25**, 261 (1876).

[2] D. Lohse, Annu. Rev. Fluid Mech. **54**, 349 (2022).

[3] J. Kim, Int. J. Heat Fluid Flow **28**, 753 (2007).

[4] F. R. Smith, C. Nicloux, and D. Brutin, Phys. Rev. Fluids **3**, 013601 (2018).

[5] C. Josserand and S. T. Thoroddsen, Annu. Rev. Fluid Mech. **48**, 365 (2016).

[6] A. L. Yarin, Annu. Rev. Fluid Mech. **38**, 159 (2006).

[7] A. L. Yarin, I. V. Roisman, and C. Tropea, *Collision Phenomena in Liquids and Solids* (Cambridge University Press, Cambridge, England, 2017).

[8] M. A. Nearing, J. M. Bradford, and R. D. Holtz, Soil Sci. Soc. Am. J. **50**, 1532 (1986).

[9] M. Ahmad, M. Schatz, and M. V. Casey, Wear **303**, 83 (2013).

[10] B. Amirzadeh, A. Louhghalam, M. Raessi, and M. Tootkaboni, J. Wind Eng. Ind. Aerodyn. **163**, 33 (2017).

[11] O. Gohardani, Prog. Aerosp. Sci. **47**, 280 (2011).

[12] X. Cheng, T.-P. Sun, and L. Gordillo, Annu. Rev. Fluid Mech. **54** (2021).

[13] J. Li, B. Zhang, P. Guo, and Q. Lv, J. Appl. Phys. **116**, 214903 (2014).

[14] D. Soto, A. B. De Lariviere, X. Boutillon, C. Clanet, and D. Quéré, Soft Matter **10**, 4929 (2014).

[15] J. Philippi, P.-Y. Lagrée, and A. Antkowiak, J. Fluid Mech. **795**, 96 (2016).

[16] B. Zhang, J. Li, P. Guo, and Q. Lv, Exp. Fluids **58**, 125 (2017).

[17] L. Gordillo, T.-P. Sun, and X. Cheng, J. Fluid Mech. **840**, 190 (2018).

[18] B. R. Mitchell, J. C. Klewicki, Y. P. Korkolis, and B. L. Kinsey, J. Fluid Mech. **867**, 300 (2019).

[19] R. Zhang, B. Zhang, Q. Lv, J. Li, and P. Guo, Exp. Fluids **60**, 64 (2019).

[20] H. Wagner, Z. Angew. Math. Mech. **12**, 193 (1932).

[21] S. Wildeman, C. W. Visser, C. Sun, and D. Lohse, J. Fluid Mech. **805**, 636 (2016).

[22] V. Bergeron and D. Quéré, Phys. World **14**, 27 (2001).

[23] D. Bartolo, C. Josserand, and D. Bonn, Phys. Rev. Lett. **96**, 124501 (2006).

[24] D. Richard, C. Clanet, and D. Quéré, Nature (London) **417**, 811 (2002).

[25] T. Onda, S. Shibuichi, N. Satoh, and K. Tsujii, Langmuir **12**, 2125 (1996).

[26] A. Lafuma and D. Quéré, Nat. Mater. **2**, 457 (2003).

[27] A. Tuteja, W. Choi, M. Ma, J. M. Mabry, S. A. Mazzella, G. C. Rutledge, G. H. McKinley, and R. E. Cohen, Science **318**, 1618 (2007).

[28] H. J. Cho, D. J. Preston, Y. Zhu, and E. N. Wang, Nat. Rev. Mater. **2**, 16092 (2017).

[29] M. Liu, S. Wang, and L. Jiang, Nat. Rev. Mater. **2**, 17036 (2017).

[30] C. Hao, Y. Liu, X. Chen, J. Li, M. Zhang, Y. Zhao, and Z. Wang, Small **12**, 1825 (2016).

[31] S. Wu, Y. Du, Y. Alsaid, D. Wu, M. Hua, Y. Yan, B. Yao, Y. Ma, X. Zhu, and X. He, Proc. Natl. Acad. Sci. U.S.A. **117**, 11240 (2020).

[32] H. Zhan, C. Lu, C. Liu, Z. Wang, C. Lv, and Y. Liu, Phys. Rev. Lett. **126**, 234503 (2021), no force measurements were provided in this Letter.

[33] M. Callies and D. Quéré, Soft Matter **1**, 55 (2005).

[34] M. Sbragaglia, A. M. Peters, C. Pirat, B. M. Borkent, R. G. H. Lammertink, M. Wessling, and D. Lohse, Phys. Rev. Lett. **99**, 156001 (2007).

[35] Y. Li, D. Quéré, C. Lv, and Q. Zheng, Proc. Natl. Acad. Sci. U.S.A. **114**, 3387 (2017).

[36] P. Tsai, R. G. H. Lammertink, M. Wessling, and D. Lohse, Phys. Rev. Lett. **104**, 116102 (2010).

[37] X. Chen, R. Ma, J. Li, C. Hao, W. Guo, B. L. Luk, S. C. Li, S. Yao, and Z. Wang, Phys. Rev. Lett. **109**, 116101 (2012).

[38] P. Papadopoulos, L. Mammen, X. Deng, D. Vollmer, and H.-J. Butt, Proc. Natl. Acad. Sci. U.S.A. **110**, 3254 (2013).

[39] E. Bormashenko, R. Pogreb, G. Whyman, and M. Erlich, Langmuir **23**, 12217 (2007).

[40] D. Bartolo, F. Bouamrirene, E. Verneuil, A. Buguin, P. Silberzan, and S. Moulinet, Europhys. Lett. **74**, 299 (2006).

[41] D. Lohse, R. Bergmann, R. Mikkelsen, C. Zeilstra, D. van der Meer, M. Versluis, K. van der Weele, M. van der Hoef, and H. Kuipers, Phys. Rev. Lett. **93**, 198003 (2004).

[42] D. Lohse, Phys. Rev. Fluids **3**, 110504 (2018).

[43] S.-H. Lee, M. Rump, K. Harth, M. Kim, D. Lohse, K. Fezzaa, and J. H. Je, Phys. Rev. Fluids **5**, 074802 (2020).

[44] S. Mitra, Q. Vo, and T. Tran, Soft Matter **17**, 5969 (2021).

[45] S. Popinet and Collaborators, Basilisk C: Volume of Fluid method, http://basilisk.fr (last accessed December 8, 2021) (2013–2022).

[46] A. Gauthier, S. Symon, C. Clanet, and D. Quéré, Nat. Commun. **6**, 8001 (2015).

[47] O. Ramírez-Soto, V. Sanjay, D. Lohse, J. T. Pham, and D. Vollmer, Sci. Adv. **6**, eaba4330 (2020).

[48] See Supplemental Material at http://link.aps.org/supplemental/10.1103/PhysRevLett.129.104501, which includes Refs. [49–74], for a description of experimental and numerical methods, comparison of impact forces on hydrophilic and superhydrophobic substrates, some notes on various regimes, and calculations of Worthington jet and drop retraction characteristics. Also, see Supplemental Movies 1–6.

[49] S. Popinet, Annu. Rev. Fluid Mech. **50**, 49 (2018).

[50] S. Popinet and Collaborators, Basilisk C: Reduced pressure library, http://basilisk.fr/src/reduced.h (last accessed February 4, 2022) (2013–2022).

[51] G. Tryggvason, R. Scardovelli, and S. Zaleski, *Direct Numerical Simulations of Gas–Liquid Multiphase Flows* (Cambridge University Press, Cambridge, England, 2011).

[52] A. Prosperetti and G. Tryggvason, *Computational Methods for Multiphase Flow* (Cambridge University Press, Cambridge, England, 2009).

[53] J. U. Brackbill, D. B. Kothe, and C. Zemach, J. Comput. Phys. **100**, 335 (1992).

[54] S. Popinet, J. Comput. Phys. **228**, 5838 (2009).

[55] S. Popinet and Collaborators, Basilisk C: Surface tension library, http://basilisk.fr/src/tension.h (last accessed January 11, 2022) (2013–2022).

[56] L. D. Landau and E. M. Lifshitz, *Fluid Mechanics: Course of Theoretical Physics*, 2nd ed. (Elsevier, New York, 1987), Vol. 6.

[57] V. Sanjay, Impact forces of water drops falling on superhydrophobic surfaces, https://github.com/VatsalSy/Impact-forces-of-water-drops-falling-on-superhydrophobic-surfaces.git (last accessed February 4, 2022) (2022).

[58] W. Bouwhuis, R. C. A. van der Veen, T. Tran, D. L. Keij, K. G. Winkels, I. R. Peters, D. van der Meer, C. Sun, J. H. Snoeijer, and D. Lohse, Phys. Rev. Lett. **109**, 264501 (2012).

[59] R. C. A. van der Veen, T. Tran, D. Lohse, and C. Sun, Phys. Rev. E **85**, 026315 (2012).

[60] S.-H. Lee, K. Harth, M. Rump, M. Kim, D. Lohse, K. Fezzaa, and J. H. Je, Soft Matter **16**, 7935 (2020).

[61] P. Chantelot and D. Lohse, J. Fluid Mech. **928**, A36 (2021).

[62] B. R. Mitchell, A. Nassiri, M. R. Locke, J. C. Klewicki, Y. P. Korkolis, and B. L. Kinsey, in *International Manufacturing Science and Engineering Conference* (American Society of Mechanical Engineers, LA USA, 2016), Vol. 49897, p. V001T02A047.

[63] Y. Renardy, S. Popinet, L. Duchemin, M. Renardy, S. Zaleski, C. Josserand, M. A. Drumright-Clarke, D. Richard, C. Clanet, and D. Quéré, J. Fluid Mech. **484**, 69 (2003).

[64] A. S. Grinspan and R. Gnanamoorthy, Colloids Surf. A **356**, 162 (2010).

[65] B. Samuel, H. Zhao, and K.-Y. Law, J. Phys. Chem. C **115**, 14852 (2011).

[66] V. Liimatainen, M. Vuckovac, V. Jokinen, V. Sariola, M. J. Hokkanen, Q. Zhou, and R. H. A. Ras, Nat. Commun. **8**, 1798 (2017).

[67] J. Eggers, M. A. Fontelos, C. Josserand, and S. Zaleski, Phys. Fluids **22**, 062101 (2010).

[68] G. Riboux and J. M. Gordillo, Phys. Rev. Lett. **113**, 024507 (2014).

[69] D. Bartolo, C. Josserand, and D. Bonn, J. Fluid Mech. **545**, 329 (2005).

[70] J.-L. Pierson, J. Magnaudet, E. J. Soares, and S. Popinet, Phys. Rev. Fluids **5**, 073602 (2020).

[71] H. Deka and J.-L. Pierson, Phys. Rev. Fluids **5**, 093603 (2020).

[72] C. Clanet, C. Béguin, D. Richard, and D. Quéré, J. Fluid Mech. **517**, 199 (2004).

[73] N. Laan, K. G. de Bruin, D. Bartolo, C. Josserand, and D. Bonn, Phys. Rev. Applied **2**, 044018 (2014).

[74] C. W. Visser, P. E. Frommhold, S. Wildeman, E. Mettin, D. Lohse, and C. Sun, Soft Matter **11**, 1708 (2015).

[75] Lord Rayleigh, Proc. R. Soc. London, Ser. A **29**, 71 (1879).

[76] P. Chantelot, Rebonds spéciaux de liquides, Ph.D. thesis, Université Paris-Saclay (ComUE), 2018.

[77] D. Richard and D. Quéré, Europhys. Lett. **50**, 769 (2000).

[78] A. Woodcock, C. Kientzler, A. Arons, and D. Blanchard, Nature (London) **172**, 1144 (1953).

[79] V. Sanjay, D. Lohse, and M. Jalaal, J. Fluid Mech. **922**, A2 (2021).

[80] J. Moláček and J. W. Bush, Phys. Fluids **24**, 127103 (2012).

[81] L. Xu, W. W. Zhang, and S. R. Nagel, Phys. Rev. Lett. **94**, 184505 (2005).

[82] A. Jha, P. Chantelot, C. Clanet, and D. Quéré, Soft Matter **16**, 7270 (2020).

[83] D. Quéré, Annu. Rev. Fluid Mech. **45**, 197 (2013).